Journal of Nuclear Materials 389 (2009) 436–442

Contents lists available at ScienceDirect

Journal of Nuclear Materials

journal homepage: www.elsevier.com/locate/jnucmat

Crystallographic measurement of the β to α phase transformation and δ-hydride precipitation in a laser-welded Zircaloy-2 tube by electron backscattering diffraction

K. Une *, S. Ishimoto

Nippon Nuclear Fuel Development Co. Ltd., 2nd Research Department, 2163 Oarai-machi, Narita-cho, Higashi-Ibaraki-Gun, Ibaraki-ken, Ibaraki 311-1313, Japan

ARTICLE INFO

Article history:
Received 30 September 2008
Accepted 18 February 2009

ABSTRACT

Crystallographic measurement of the β to α phase transformation and δ-hydride precipitation in a laser-welded Zircaloy-2 ferrule tube were carried out using an electron backscattering diffraction pattern (EBSP). A basket-weave structure with sub-micron lath width caused by quenching from the β to α phase was observed in the heat-affected and fusion zones, and mainly showed a grain boundary misorientation angle of 60° with an <11$\bar{2}$0> rotation axis. This result is consistent with the Burgers orientation relationship of $\{1\,1\,0\}_\beta//(0\,0\,0\,1)_\alpha$ and $<1\,1\,1>_\beta//<1\,1\,\bar{2}\,0>_\alpha$ for the β to α phase transformation. The texture of the quenched α′ phase was strongly inherited from the original α phase, having a radial (0001) basal pole and axial {11$\bar{2}$0} textures, even in the fusion zone. The primary hydride habit plane in the welded Zircaloy-2 was $(0\,0\,0\,1)_\alpha//\{1\,1\,1\}_\delta$, matching previously obtained results for recrystallized cladding tubes. In addition to the primary habit plane, secondary habit planes were observed for the other low-index planes {10$\bar{1}$0} and {10$\bar{1}$1} in the fusion zone. The heterogeneous accumulation of hydrides in the transition zone between heat-affected and unaffected zones was mainly due to the residual stress distribution in the narrow region.

1. Introduction

Hydride-related embrittlement of Zr-alloy fuel cladding and spacer is an important issue limiting light water reactor fuel performance at high burnup. Indeed, outside-in cracking of high burnup BWR claddings has been observed at power ramp tests [1]. Although no such fuel spacer failure has yet been reported, the performance of fuel spacers with high hydrogen concentrations should be investigated. This investigation should include the integrity of the fuel assembly during reactor operation as well as during post-operation handling [2].

There are many weld locations in a fuel spacer, so spacer microstructure varies with position, drastically changing depending on the distance from a welding center. In the fusion and heat-affected zones, $\alpha \rightarrow \beta \rightarrow (\text{molten state} \rightarrow \beta) \rightarrow \alpha'$ or $\alpha \rightarrow (\alpha + \beta) \rightarrow \alpha'$ phase transformations occur. There have been many reported microstructural investigations by optical and scanning electron microscopy which focused on the metallographic morphology of the transformed phases [3–8]. However, there have been few crystallographic examinations reported. From earlier X-ray examinations of single-crystal Zr, an important crystal orientation relationship (Burgers relation) was derived for the β to α′ phase transformation [9,10]. Theoretical [11] and experimental examinations [12] of the texture change after $\alpha \rightarrow \beta \rightarrow \alpha'$ transformation in zirconium crystals were performed. More recently, crystallographic investigations of the phase transformation in Zircaloy-4 were carried out, using an electron backscattering diffraction pattern (EBSP) and focusing on inherited texture [13]. However, the crystallographic nature of the quenched-lath structure has not been made clear, because of the limited spatial resolution used in the EBSP measurements. For the precipitation of δ-hydrides in the transformed phase, microstructural observations have been reported [14]. However, there has been little crystallographic study of the hydride habit plane or of precipitation sites in the quenched phase, despite much crystallographic examination of the α annealed phase, such as our previous EBSP investigations [15,16].

In this study, crystallographic data of the $\beta \rightarrow \alpha'$ transformed phase and δ-hydride in laser-welded Zircaloy-2 ferrule tube were obtained using a high-resolution EBSP technique. From crystal orientation maps of the transformed phase as well as hydride and pole figure analysis, crystallographic details of the quenched-lath structure and hydride habit plane were elucidated. Moreover, the cause of heterogeneous accumulation of hydrides was sought by measuring macroscopic residual-stress distribution using X-ray diffractometry.

* Corresponding author.
E-mail address: une@nfd.co.jp (K. Une).

0022-3115/$ - see front matter © 2009 Elsevier B.V. All rights reserved.
doi:10.1016/j.jnucmat.2009.02.033

2. Experimental

2.1. Specimen

Specimens examined in the present EBSP measurements were prepared by welding two Zircaloy-2 ferrule tubes with a recrystallized α-grain structure, using a CO_2 laser. The tube reduction and annealing process was almost the same as those of Zircaloy-2 cladding tubes. The Zircaloy-2 alloy compositions were 1.37 Sn, 0.17 Fe, 0.11 Cr, and 0.07 Ni by wt%, with the balance Zr. After welding, the specimen tubes were hydrogenated in LiOH solution at 315 °C for 24 h, then the tubes were cut longitudinally, as shown in Fig. 1.

Optical micrographs after hydride etching and sectioning the tube in the radial–axial plane are shown in Fig. 1. The precipitation morphology of hydrides is significantly different in each of the following four zones: fusion, heat-affected, transition, and unaffected. Larger hydrides of several tens to 100 μm in size appeared to precipitate randomly in the fusion and heat-affected zones. On the contrary, in the unaffected zone, axially-oriented (or circumferentially-oriented) hydrides were found, as seen in Zircaloy-2 cladding tubes [15,16]. In the transition region between the heat-affected and unaffected zones, a heterogeneous accumulation of hydrides was observed. Though the hydrogen concentrations of each zone were not determined, an average concentration in the present welded specimen was 150–200 ppm. The final surface treatment of polished samples for EBSP mapping was carried out by electropolishing in a solution of 6% $HClO_4$, 35% $CH_3(CH_2)_2CH_2OH$ and 59% CH_3COOH.

2.2. EBSP measurements

Crystallographic orientation measurements of welded specimens cross-sectioned in the radial–axial plane were made using a field emission scanning electron microscope (FE-SEM, JEOL-JSM6500F) equipped with an EBSP system (TSL-OIM). The estimated diameter of the electron beam at an acceleration voltage of 20 kV and a probe current of 1.5 nA was about 20 nm, and the scanning step for EBSP mapping was 50 nm. Mapping data were obtained for the four representative zones. The mapping area was about 15 × 30 μm for the fusion zone, and about 20 × 20 μm for the other zones. From the EBSP data of α-Zr and δ-ZrH_x, various analyses of image quality map, crystal orientation and direction maps, direct and inverse pole figures, and grain boundary characteristics were derived. The relationship of crystallographic orientation between hydrides and the grains of the surrounding Zr matrix was evaluated by a direct pole figure plot of the Zr matrix and hydride phases at each analysis point [15,16].

2.3. X-ray diffractometry

Residual stresses in the welded specimen were measured by an X-ray diffractometer (JEOL-JDX-8030) using the conventional $2\theta - \sin^2\psi$ plot method. In the present measurements, Cr-Kα of 30 mA at 40 kV and the reflection peak of $(20\bar{2}2)$ from hcp Zr ($2\theta = 137.17°$) were employed. In the calculation of residual stress, the mechanical properties of Young's modulus: 97.2 GPa and Poisson's ratio: 0.293 were used [17].

3. Results and discussion

3.1. Crystallography of the β to α transformation

All EBSP data were obtained from the radial direction of a longitudinal section of the specimen tube. Fig. 2(a)–(d) give image quality (IQ) maps of the four zones: unaffected, transition (between unaffected and heat-affected), heat-affected, and fusion. The IQ map is formed by mapping an image quality parameter onto a gray scale, describing the quality of the diffraction pattern at each point in an EBSP scan. The quality of diffraction pattern is dependent on the perfection of the crystal lattice in the diffracting volume. Thus, the image quality in strained locations containing many dislocations, grain and sub-grain boundaries with the mixed diffraction patterns from the two grains, as well as segregated precipitates, becomes lower. The corresponding inverse pole figure (IPF) maps of α-Zr grains (// radial direction) are shown in Fig. 3(a)–(d). Each grain color in the maps is coordinated with the stereographic triangle $(0001)/\{10\bar{1}0\}/\{2\bar{1}\bar{1}0\}$ of the hexagonal structure. Black and white lines denote high-angle (>15°) and low-angle grain boundaries (5–15°), and black regions correspond to δ-ZrH_x grains.

The IQ and IPF maps in the unaffected and transition zones of the present ferrule tubes correspond well to previous EBSP results for recrystallized Zircaloy-2 cladding tubes [15,16], because the tubes are fabricated by similar methods. One difference is that the equiaxed grain size in the transition zone (3.5 μm) is somewhat larger than in the unaffected zone (2.8 μm). The latter grain size is in good accordance with that of cladding tubes [16]. The IQ and IPF maps in the heat-affected and fusion zones are quite different from the previous two zones. In these β quenched zones, a so-called Widmanstatten structured α′ platelet phase is clearly evident. In the heat-affected zone, this phase is composed of two regions: basket-weave (prior-β1) and quasi parallel-plate α′ structures (prior-β2). The basket-weave structure is observed over almost the entire fusion zone. The parallel-plate structure is formed on one habit plane of prior-β grain at the parent grain

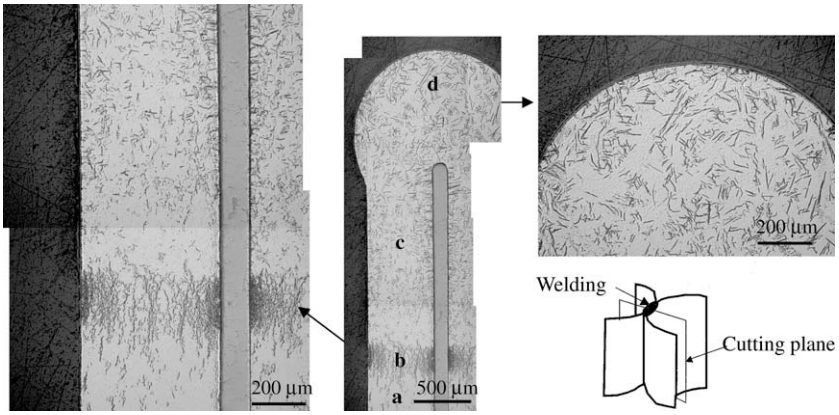

Fig. 1. Metallograph of laser-welded Zircaloy-2 tube in a longitudinal section. (a) Unaffected zone; (b) transient zone; (c) heat-affected zone and (d) fusion zone.

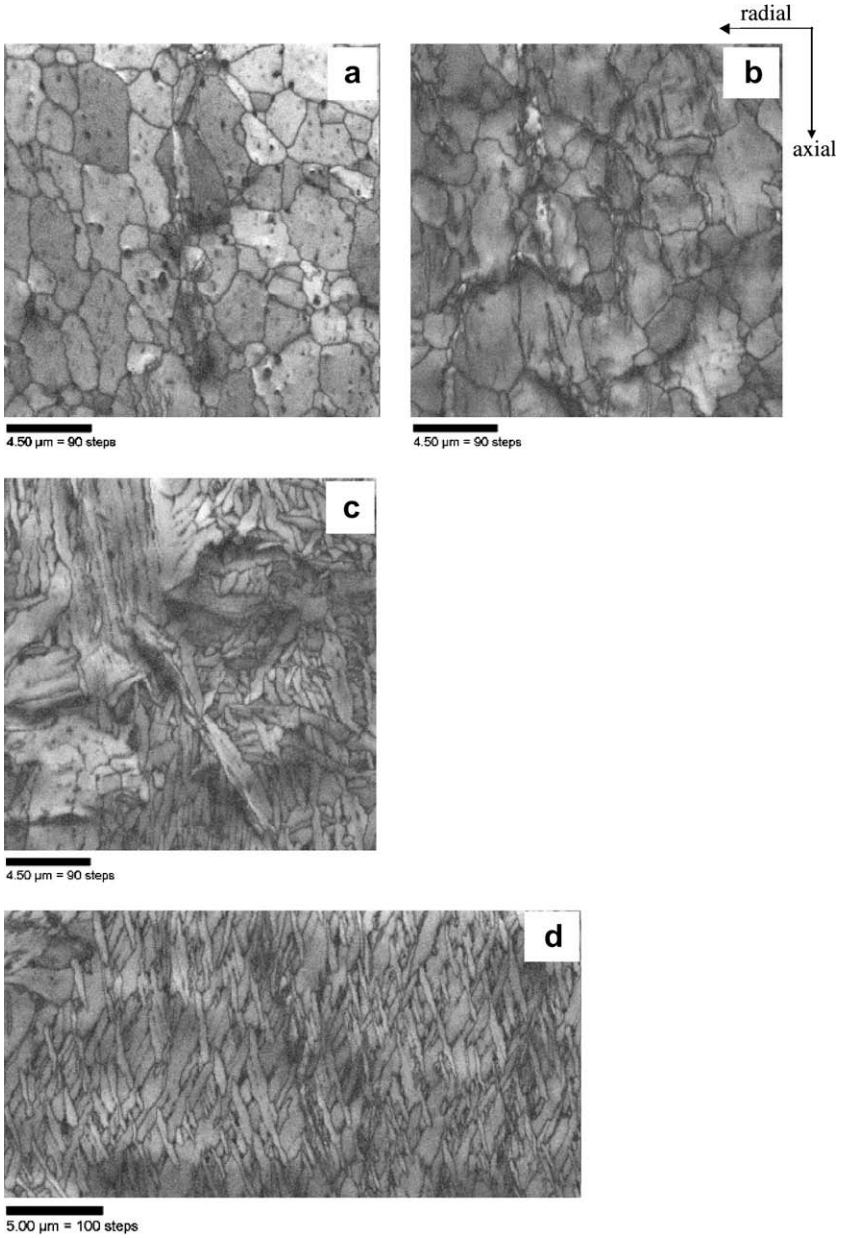

Fig. 2. Image quality (IQ) maps of laser-welded Zircaloy-2 tube. (a) Unaffected zone; (b) transition zone; (c) heat-affected zone and (d) fusion zone.

boundaries, while the basket-weave (nonparallel) structure results from the random precipitation of α' plates on a number of planes in a prior-β grain [7]. In fact, the quasi parallel-plate structure in Fig. 3(c) has the same crystal orientation. The lath boundary, not sub-grain boundary, seen in the IQ maps of Fig. 2(c) and (d) with the same crystal orientation probably results from small second-phase particles (SPP) which align during the phase transformation, because the quantity of nucleation sites for the α' plates has been related to the abundance of SPP, composed of low solubility elements in the β phase [6,8].

Variation of the quenched microstructure has been also related to the cooling rate from the β phase [7]. A faster cooling rate of 10–600 °C/s favors the basket-weave structure, while the parallel-plate structure is formed by cooling rates of <10 °C/s. At very fast cooling rates of >1600–2000 °C/s, the martensitic acicular structure is formed. Though the accurate temperature transient in the fusion zone is unknown, the cooling rate may be inferred to be above several 10's of °C/s from the existence of the basket-weave structure and the lath width of about 0.5–1.0 μm in the fusion zone, based on the reported correlation between cooling rate and lath width [3].

Fig. 4(a)–(c) show the (0001) and $\{11\bar{2}0\}$ pole figures obtained by EBSP for the unaffected, heat-affected, and fusion zones, respectively. The unaffected zone, as well as the transition zone, has a strong radial texture of the (0001) basal pole, with projections tilted from the radial to the circumferential direction in the range from 0° to 50°. This radial texture of the basal pole is similar to that of recrystallized Zircaloy-2 cladding tubes [15,16], because they have a similar reduction schedule to the present ferrule tube. Furthermore, an axial $\{11\bar{2}0\}$ texture is observed. Namely, the analysis of all the acquired EBSP maps shows that the fraction of the $<11\bar{2}0>$//AD fiber within 15° was 65.4%. Compared to these original textures, the basal pole projections in the heat-affected and fusion zones become much more concentrated, and the $\{11\bar{2}0\}$ axial texture remains valid, even in the fusion zone. The fractions of the $<11\bar{2}0>$//AD fiber within 15° were 58.2% in the heat-affected zone

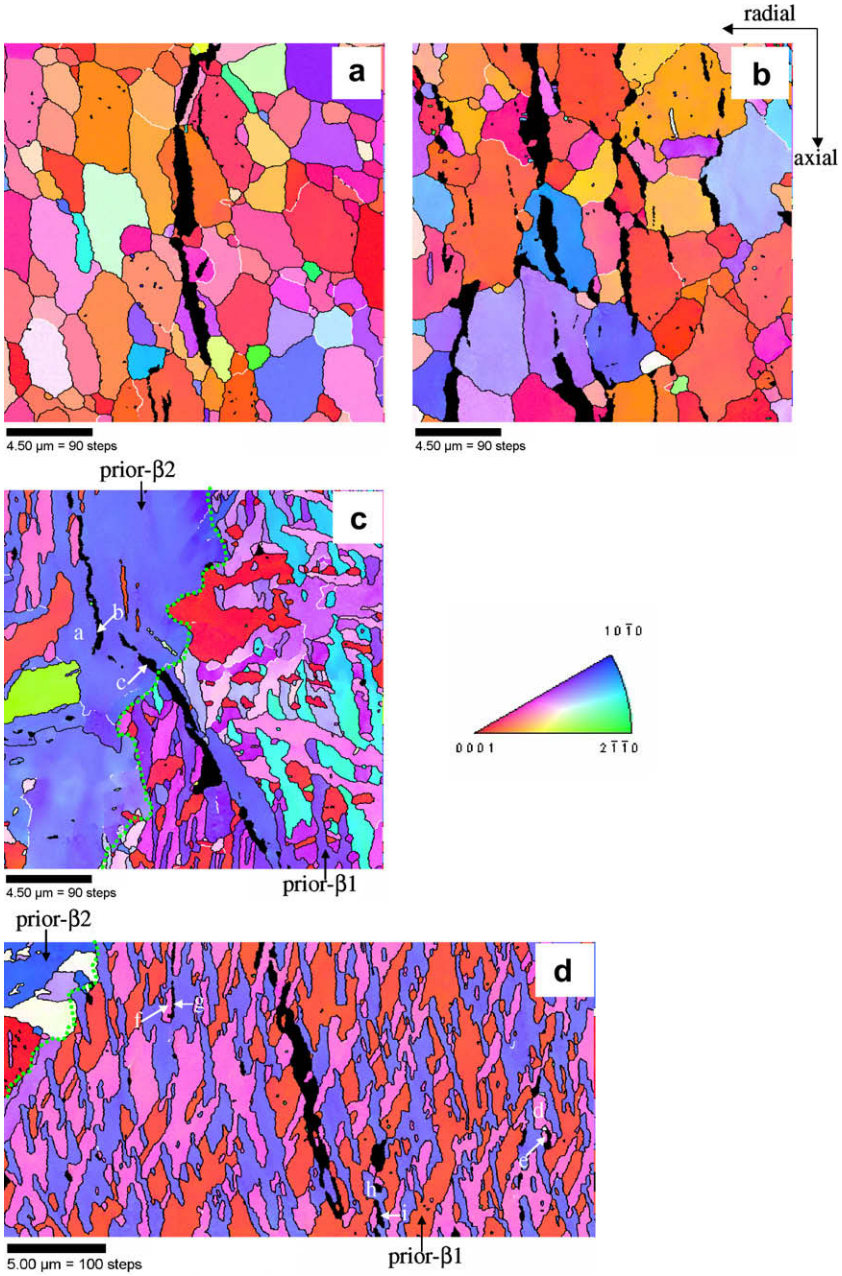

Fig. 3. Inverse pole figure (IPF) maps of laser-welded Zircaloy-2 tube (// radial direction). (a) Unaffected zone; (b) transition zone; (c) heat-affected zone and (d) fusion zone. Black and white lines denote high-angle (>15°) and low-angle grain boundaries (5–15°), and black regions correspond to δ-ZrH_x grains. Dotted green line is the boundary of two prior-β colonies.

and 97.2% in the fusion zone. The basal pole figures in these β quenched zones are a consequence of variant selection of crystal orientation during the transformation. The concentrated projections of the basal pole are fairly consistent with the distributions of grain boundary misorientation angles in Fig. 5. The original α-grain structure has a wide variation of misorientation angle from 5° to 90°. On the other hand, in the heat-affected and fusion zones, the misorientation angles are concentrated at 60° ± 5° with a rotation axis of <11$\bar{2}$0>, and additionally at 90° ± 5° in the heat-affected zone. This implies that the α′ platelet grains preferentially nucleate and grow with crystal orientations of 60° and 90°.

In the IPF map of the heat-affected zone (Fig. 3(c)), it is obvious that the mapping area is divided into two prior-β colonies inherited from different parent grains. Dotted green line is the boundary of the two colonies. In both colonies, the crystal orientation relationship of the basal pole with 60° and 90° is found, as seen in Fig. 4(b). In both the prior-β1 and prior-β2 colonies, three (0001) projections separated by 60° are observed on the RD-TD plane, which are inherited from the original texture. In the IPF map of the fusion zone (Fig. 3(d)), except for the small area of prior-β2 colony at the upper left, the prior-β1 basket-weave colony consists of the quenched α′ grains with three different crystal orientations, which correspond to the three strong projections of the basal pole figure on the RD-TD plane (Fig. 4(c)). The above EBSP results are fully consistent with the Burgers orientation relation for the β (bcc) to α (hcp) phase transformation, i.e. $(0001)_\alpha$//$\{110\}_\beta$ and $<11\bar{2}0>_\alpha$//$<111>_\beta$. The habit plane of the β phase is {110} with 6-fold symmetry. Therefore, one of the six {110} planes of the β-structure becomes the (0001) plane of the α-structure, while one of the four <111> directions in the β-structure becomes one

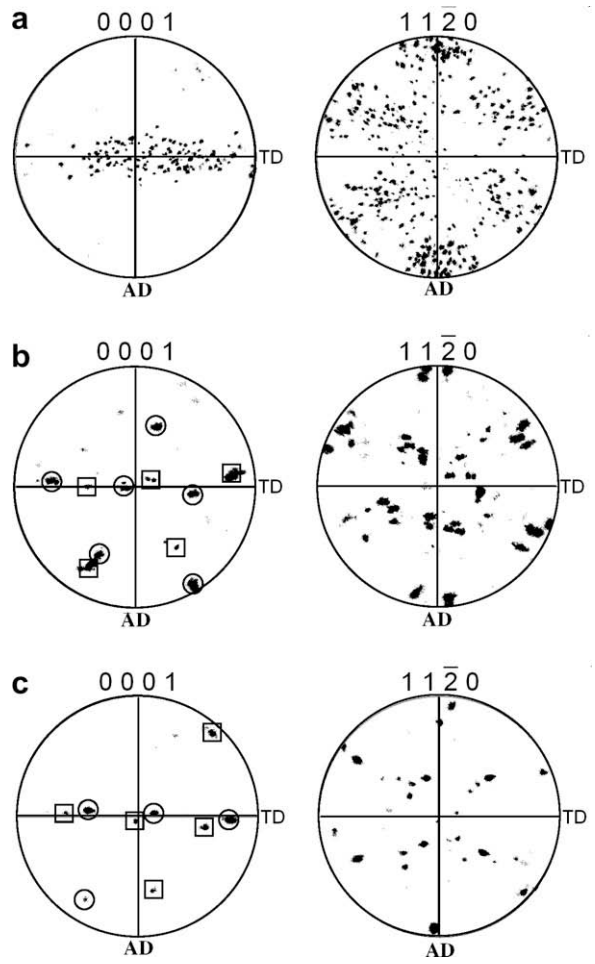

Fig. 4. (0001) and {11$\bar{2}$0} pole figures of laser-welded Zircaloy-2 tube (// radial direction). a: Unaffected zone; b: heat-affected zone; c: fusion zone. (0001) projections marked by 'circles' and 'squares' in the heat-affected and fusion zones are the reflections from prior-β1 and prior-β2 grains, respectively.

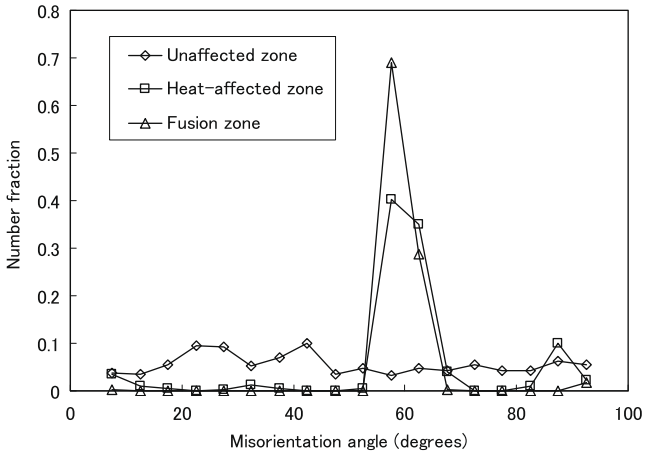

Fig. 5. Grain boundary misorientation angle of laser-welded Zircaloy-2 tube.

of the <11$\bar{2}$0>$_\alpha$ directions in the α-structure [9,10]. The angles between {1 1 0}$_\beta$ planes are 60° and 90°, and are reflected on the projections of the basal pole figures in Fig. 4(b) and (c). Namely, three of the six {1 1 0} planes with the same zone axis align at the interval of 60° on the RD-TD plane. In the phase transformations of α → β → (molten state) → β → α′, the strong <11$\bar{2}$0>$_\alpha$//AD was found in both the original α- and quenched α′-structures, even in the fusion zone. This implies that the parent β grains also have a strong <1 1 1>$_\beta$//AD. One possible explanation for the texture inheritance in the fusion zone is that a successive solidification of the molten Zircaloy starting from the edge of the heat-affected zone with the strongly textured β grains, controls the crystal orientations in the phase transformation of molten state → β → α′.

3.2. Hydride habit plane

Hydride platelets (black regions in Fig. 3) in the welded Zircaloy-2 specimen precipitate in both grains and grain boundaries along the axial direction in the radial–axial plane of the tube. The equivalent grain size is 0.9–1.8 μm and the width of the platelets is 0.3–1.0 μm. These hydride morphologies are similar to the α-annealed recrystallized structure of Zircaloy-2 cladding tube [15,16]. A remarkable difference between unaffected and transition zones is the number of hydrides precipitated, despite their very similar α-annealed structures. In the latter zone, a much larger number of hydrides are precipitated.

The hydride habit plane, or the crystallographic relationship between micron-sized hydrides and the surrounding Zr grains, in the four zones was surveyed using the same pole figure method employed in our previous reports [15,16]. The crystal planes examined were (0001), {10$\bar{1}$7}, {10$\bar{1}$1}, and {10$\bar{1}$0} for α-Zr matrix grains, and {1 1 1}, {1 0 0}, and {1 1 0} for the δ-hydride grains. Coincidence of the crystallographic orientation of the hydrides and Zr grains was judged by a difference in angles of <±5°.

In the equiaxed α-grain structure of the unaffected and transition zones, the orientation relation of $(0001)_\alpha//\{111\}_\delta$ was confirmed for almost all cases at dozens of analysis locations (probability: >93%), which is in good accordance with previous results obtained for recrystallized Zircaloy-2 cladding tubes [15,16]. In the parallel-plate α′ grain structure (prior β2 domain) and the basket-weave structure (prior β1 domain) in the heat-affected zone (Fig. 3(c)), broken hydride strings traverse the two domains. The angle between the hydride strings (denoted b and c in Fig. 3(c)) is 60° with a rotation axis of <1 1 1>, as shown in the pole figures of Fig. 6 (location (a, b, c)). These broken hydride strings precipitate with the orientation relation of $(0001)_\alpha//\{111\}_\delta$ from the coincidences of these projection angles at the locations (a, b) and (a, c), as well as other small hydrides. In the basket-weave structure of the fusion zone (Fig. 3(d)), the relation between small island-type Zr grains and surrounding hydride (location (d, e)) shows $(0001)_\alpha//\{111\}_\delta$, while for the other small hydride cases the relations of $\{10\bar{1}1\}_\alpha//\{111\}_\delta$ (location (f, g)) and $\{10\bar{1}0\}_\alpha//\{110\}_\delta$ (location (h, i)) are also valid, as shown in Fig. 6. The latter two relations for hydride habit plane have been reported in the literature [18,19].

The heterogeneous accumulation of hydrides in the transition zone (see Fig. 1) appears to be similar to that observed in Zr liner cladding tubes, in which hydrides accumulate nonuniformly in the Zr liner region adjacent to the Zr liner/Zircaloy-2 interface. This phenomenon can be clearly explained by the difference in the terminal solid solubility of hydrogen between Zircaloy-2 and pure Zr [20]. Hydride precipitation and growth arise preferentially in the pure Zr liner because of its lower hydrogen solubility. In the present welded Zircaloy-2, there was no significant difference in alloy element concentration, such as Sn, or in texture between the unaffected and transition zones. Moreover, no heterogeneous accumulation of hydrides in the transition zone was confirmed for the welded specimens after stress relief annealing at 500–577 °C. Consequently, the residual stress distribution in welded specimens is most likely responsible for the heterogeneous hydride accumulation in the transition zone. For example, relatively larger tensile stresses were measured near the fusion center, or at a particular

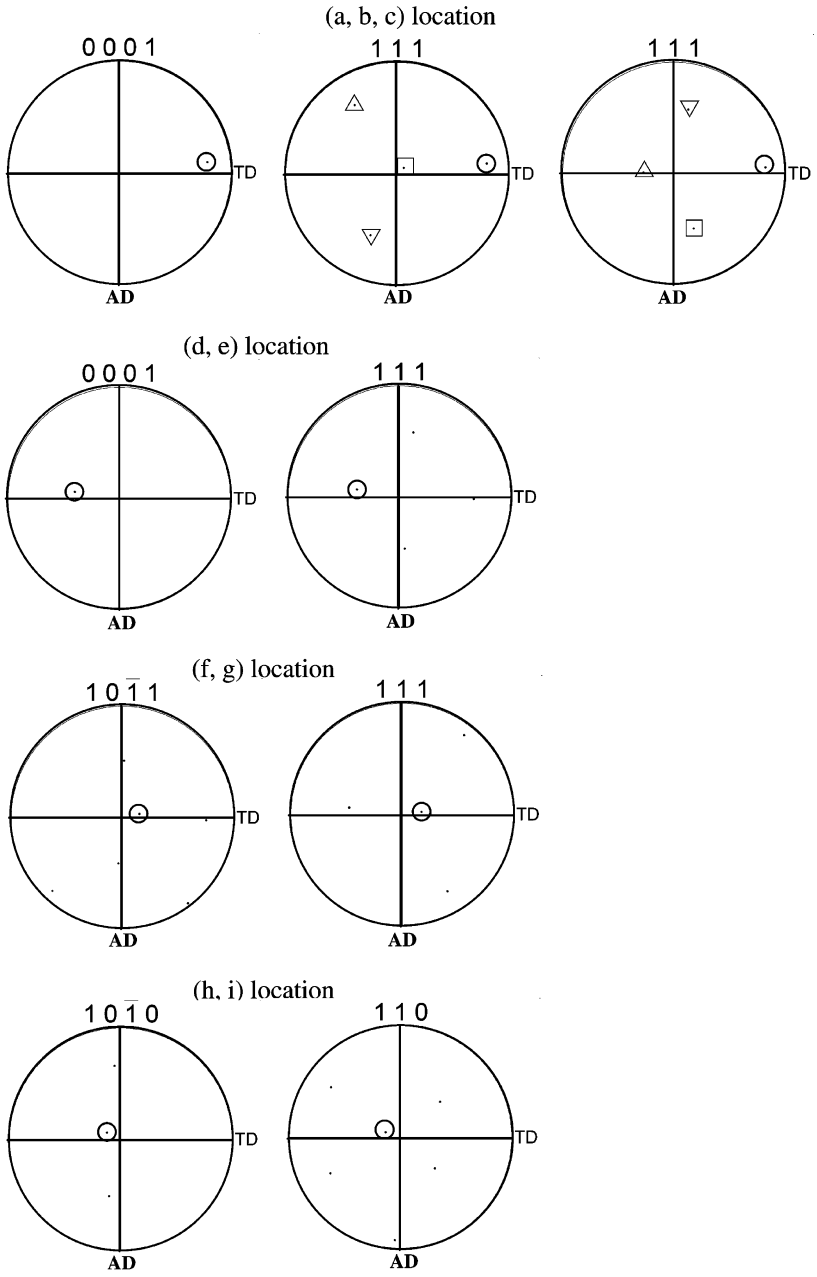

Fig. 6. Pole figure analysis results of α-Zr and δ-ZrH_x for determination of hydride habit plane in the heat-affected ((a, b, c) location) and fusion zones ((d, e), (f, g), (h, i) locations). Circles in the pole figures denote the coincidence of crystallographic orientations.

distance from it, in welded Zircaloy specimens [21,22]. The lowering of the hydrogen solubility by tensile stress has been experimentally demonstrated [23].

Fig. 7 shows a residual stress distribution along the axial direction in the present welded tube, as measured by X-ray diffractometry. The measurements were made on the inner surface of the longitudinal specimen. In the fusion and heat-affected zones, the data vary from zero to tensile stress region. In the transition zone between the unaffected and heat-affected zones, the sign of residual stress abruptly changes from tension (≈120 MPa) to compression (≈150 MPa) over a narrow region. Then the residual stress gradually approaches zero in the unaffected zone. In this narrow transition zone, heterogeneous hydride accumulation would be driven by tensile stress-induced lowering of hydrogen solubility during the hydrogenation and cooling periods. In fact, few hydrides are seen in the heat-affected zone just adjacent to the transition zone. The residual stress distribution is caused by a significant

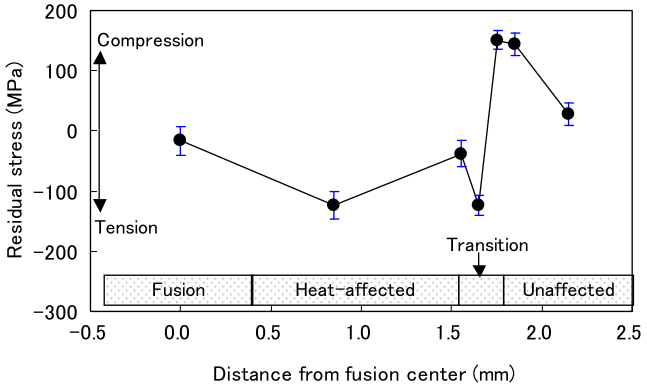

Fig. 7. Residual stress distributions in laser-welded Zircaloy-2 tube by X-ray diffractometry. Measurements were taken at the inner surface and at the center of the longitudinal section of the specimen.

difference in thermal expansion between the unaffected and heat-affected zones during cooling after welding.

4. Conclusions

Crystallographic measurements in laser-welded Zircaloy-2 ferrule tubes, focusing on the β to α phase transformation and δ-hydride precipitation in the quenched β phase, were made using EBSP. Furthermore, the macroscopic residual stress distribution was evaluated by X-ray diffraction. The data were obtained in the following four zones: unaffected, transition, heat-affected, and fusion.

(1) The α grain structure and texture of the unaffected and transition zones were almost the same as previously observed in Zircaloy-2 cladding tubes. The equiaxed α grain size in the transition zone was 3.5 μm, slightly larger than that observed (2.8 μm) in the unaffected zone. Both zones show a strong (0001) radial texture and an $\{11\bar{2}0\}$ axial texture.

(2) From the image quality (IQ) maps, the parallel and basket-weave α′ plates with sub-micron lath width were detected in the heat-affected and fusion zones experiencing β to α transformation. The lath boundary, not sub-grain boundary, observed in the IQ maps having identical crystal orientations was attributed to linear alignment of small second-phase particles. The (0001) and $\{11\bar{2}0\}$ textures of the quenched α′ lath phase were strongly inherited from the original α grain texture, even in the fusion zone. The texture inheritance in the fusion zone was probably attributed to a successive solidification of the molten Zircaloy starting from the edge of the heat-affected zone with the textured β grains, which controlled the crystal orientations in the phase transformation of molten state → β → α′.

(3) The misorientation angles of grain boundaries in the heat-affected zone were concentrated mainly at 60° and partially at 90°, while those in the fusion zone were mostly at 60° to the <11$\bar{2}$0> rotation axis. This result was fairly consistent with the Burgers orientation relation of $\{110\}_\beta//(0001)_\alpha$ and $<111>_\beta//<11\bar{2}0>_\alpha$ for the β to α phase transformation.

(4) The primary hydride habit plane in the heat-affected and fusion zones was $(0001)_\alpha//\{111\}_\delta$, as well as in the unaffected and transition zones, which was in good accordance with the previously obtained results for recrystallized Zircaloy-2 cladding tubes. Besides the primary habit plane, secondary habit planes were observed for the other low-index planes $\{10\bar{1}0\}$ and $\{10\bar{1}1\}$ in the fusion zone.

(5) The heterogeneous accumulation of hydrides in the transition zone between the unaffected and heat-affected zones was mainly due to the residual stress distribution in the narrow region, which was measured by X-ray diffractometry.

References

[1] S. Shimada, Y. Etoh, H. Hayashi, Y. Tsukuda, J. Nucl. Mater. 327 (2004) 97.
[2] Y. Hirano, Y. Mozumi, K. Kamimura, Y. Tsukuda, in: Proceedings of 2005 Water Reactor Fuel Performance Mtg., Kyoto, Japan, October 2–5, 2005.
[3] A.R. Massih, T. Andersson, P. Witt, M. Dahlback, M. Limback, J. Nucl. Mater. 322 (2003) 138.
[4] H.S. Hong, S.J. Kim, K.S. Lee, J. Nucl. Mater. 265 (1999) 108.
[5] W.M. Rumball, J. Less Common Met. 38 (1974) 233.
[6] D. Charquet, E. Alheritiere, in: Zirconium in the Nuclear Industry: Seventh International Symposium, ASTM STP 939, 1987, p. 284.
[7] T.E. Perez, M.E. Saggese, Metallography 15 (1982) 43.
[8] R.A. Holt, J. Nucl. Mater. 35 (1970) 322.
[9] W.G. Burgers, Physica 1 (1934) 561.
[10] P. Gaunt, J.W. Christian, Acta Metall. 7 (1959) 534.
[11] J.W. Glen, S.F. Pugh, Acta Metall. 2 (1954) 520.
[12] J.S. Yoo, I.S. Kim, J. Korean Nucl. Soc. 24 (1992) 75.
[13] N. Gay, M. Humbert, E. Gautier, J.L. Bechade, J. Nucl. Mater. 328 (2004) 137.
[14] S.L. Seifferi, in: Zirconium in the Nuclear Industry: Fifth International Symposium, ASTM STP 754, 1982, p. 302.
[15] K. Une, K. Nogita, S. Ishimoto, K. Ogata, J. Nucl. Sci. Technol. 41 (7) (2004) 731.
[16] K. Une, S. Ishimoto, J. Nucl. Mater. 357 (2006) 147.
[17] D. Hargman, G.A. Reymann, R. Mason, MATPRO-VERSION 11(REVISION 2), US NRC, NUREG/CR-0479 TREE-1280, 1981.
[18] J.E. Bailey, Acta Metall. 11 (1963) 267.
[19] H.M. Chung, R.S. Daum, J.M. Hiller, M.C. Billone, in: Zirconium in the Nuclear Industry: Thirteenth International Symposium, ASTM 1423, 2002, p. 561.
[20] K. Une, S. Ishimoto, J. Nucl. Sci. Technol. 41 (9) (2004) 949.
[21] C.E. Coleman, G.L. Doubt, R.W.L. Fong, J.H. Root, J.W. Bowden, S. Sagat, R.T. Webster, in: Zirconium in the Nuclear Industry: Tenth International Symposium, ASTM 1245, 1994, p. 264.
[22] D.G. Carr, M.I. Ripley, D.W. Brown, S.C. Vogel, T.M. Holden, J. Nucl. Mater. 359 (2006) 202.
[23] B.F. Kammenzind, B.M. Berquist, R. Bajaj, P.H. Kreyns, D.G. Franklin, in: Zirconium in the Nuclear Industry: Twelfth International Symposium, ASTM 1354, 2000, p. 196.